


Article

Indocyanine Green-Containing Magnetic Liposomes for Constant Magnetic Field-Guided Targeted Delivery and Theranostics

Dmitry V. Korolev ^{1,2}, Galina A. Shulmeyster ¹, Maria S. Istomina ^{1,3}, Alexey I. Nikiforov ^{1,3}, Ilia V. Aleksandrov ^{1,*} , Valentin G. Semenov ⁴ and Michael M. Galagudza ^{1,5}

¹ Institute of Experimental Medicine, Almazov National Medical Research Centre, 2 Akkuratova Street, 197341 Saint Petersburg, Russia

² Laboratory of Biophysics of Blood Circulation, Pavlov First Saint Petersburg State Medical University, 6–8 L'va Tolstogo Street, 197022 Saint Petersburg, Russia

³ Department of Micro- and Nanoelectronics, Saint Petersburg Electrotechnical University "LETI", 5 Professora Popova Street, 197376 Saint Petersburg, Russia

⁴ Institute of Chemistry, Saint Petersburg State University, 7/9 Universitetskaya Emb., 199034 Saint Petersburg, Russia

⁵ Department of Pathophysiology with Clinical Pathophysiology Course, Pavlov First Saint Petersburg State Medical University, 6–8 L'va Tolstogo Street, 197022 Saint Petersburg, Russia

* Correspondence: aleksandrov_iv@almazovcentre.ru; Tel.: +7-812-702-51-68

Abstract: The aim of the present study was to develop magnetic liposomes (MLPSs) incorporating an agent with the ability to act both as a photosensitizer and as a fluorophore for optical imaging. We therefore aimed to develop a preparation method for indocyanine green (ICG)-containing MLPS, followed by a detailed characterization of their physicochemical and magnetic properties. The ability of intravenously administered ICG-containing MLPSs to accumulate in tissue exposed to a constant magnetic field was tested in vivo. Using the thin film hydration method, 170-nm aqueous liposomes containing magnetic nanoparticles and indocyanine green were synthesized, followed by a detailed characterization of their physicochemical properties. It was shown that ICG-containing MLPSs possess the properties of T₂ contrast for MRI. Apart from this, ICG-containing MLPSs were clearly visualized using near infrared fluorescent imaging, which was demonstrated in in vivo experiments showing an accumulation of ICG-containing MLPSs in the zone of magnetic field distribution produced by a previously implanted constant magnet in the tissue. Although not directly tested in the present study, therapeutic applications of ICG-containing MLPSs include magnetic hyperthermia, as well as the photodynamic, photothermal, and photoacoustic effects of ICG. Taking into account the fact that liposomes, iron oxide nanoparticles, and ICG are all FDA-approved agents, it is highly likely that ICG-containing MLPSs could be successfully translated to clinical practice.

Keywords: magnetic liposomes; fluorophores; magnetically controlled delivery



Citation: Korolev, D.V.; Shulmeyster, G.A.; Istomina, M.S.; Nikiforov, A.I.; Aleksandrov, I.V.; Semenov, V.G.; Galagudza, M.M. Indocyanine Green-Containing Magnetic Liposomes for Constant Magnetic Field-Guided Targeted Delivery and Theranostics. *Magnetochemistry* **2022**, *8*, 127. <https://doi.org/10.3390/magnetochemistry8100127>

Academic Editor: Evgeny Katz

Received: 18 September 2022

Accepted: 12 October 2022

Published: 16 October 2022

Publisher's Note: MDPI stays neutral with regard to jurisdictional claims in published maps and institutional affiliations.



Copyright: © 2022 by the authors. Licensee MDPI, Basel, Switzerland. This article is an open access article distributed under the terms and conditions of the Creative Commons Attribution (CC BY) license (<https://creativecommons.org/licenses/by/4.0/>).

1. Introduction

Targeted drug delivery using nano-sized carriers emerged as a clinically relevant concept in the late 1980s [1,2], resulting in the rapid development of the field over the past three decades. Targeted delivery results in preferential accumulation of the drug in the area of interest, thereby both increasing its therapeutic efficacy and minimizing potential side effects on unaffected tissues [3–5]. A prototypical platform for targeted delivery is composed of a nanoparticle with an incorporated or immobilized drug. Drug delivery to the tumor tissue is achieved by using two complementary strategies, i.e., passive and active targeting. In passive targeting, drug-loaded nanoparticles accumulate within the tumor mass because of the increased permeability of atypical tumor vasculature associated with diminished lymphatic drainage [6]. While maintaining the advantage of passive targeting, active delivery could potentially provide extra tissue selectivity by means of

anchoring the nanoparticles carrying targeting ligands to the specific molecular markers expressed on cancer cells [7]. Although the most impressive results for targeted drug delivery were obtained in the field of oncology, the concept was successfully extrapolated to other local pathologies, such as myocardial ischemia–reperfusion injury [8], infectious processes [9], and inflammation [10]. Another major development occurred with the introduction of theranostics, which is a combination of targeted drug delivery and diagnostic imaging [11,12]. For attaining this purpose, the typical nanopatform is additionally supplemented with an imaging agent, which could be a radioisotope, quantum dot, MRI contrast agent, or fluorescent label.

A wide variety of materials were used to prepare nanoparticles for targeted drug delivery (for review, see [13,14] and references therein), with the initial enthusiasm about inorganic nanocarriers progressively changing to the appreciation of the advantages of organic materials, i.e., lipid-, protein-, and polysaccharide-based nanocarriers. Among lipid-based nanoparticles, liposomes are considered the most commonly used type for delivery of both hydrophilic and hydrophobic drugs [15]. Compared with other organic and especially inorganic nanoparticles, liposomes are characterized by superior drug-loading profiles, excellent biocompatibility, ease of preparation, and low immunogenicity. On one hand, surface modification of liposomes with polyethylene glycol offers the advantage of making them invisible for the macrophages of the reticuloendothelial system, thereby increasing their residence in the circulation. On the other hand, outer liposomal membrane could be doped with different targeting ligands, which is used for active liposome-mediated targeting [16]. These liposome advantages contributed to the successful clinical approval of at least 15 liposomal drug formulations intended for treatment of cancer, fungal infection, age-related macular degeneration, and chronic pain [17].

Along with conventional and stealth liposomes, magnetic liposomes (MLPSs) recently gained significant interest as delivery platforms [18]. MLPSs combine liposomes and magnetic iron oxide nanoparticles in a single nanosystem [19]. Compared with conventional liposomes, MLPSs have several advantages. First, given the presence of a strong magnetic moment, their transport to the area of interest can be additionally guided by the magnetic field. Second, moderate heating of MLPSs with an external alternating magnetic field may contribute to a controlled drug release instead of the slow and uncontrolled release observed in conventional liposomes [20]. Third, more intense external alternating magnetic field-mediated heating of MLPSs (e.g., up to 43–45 °C) can be used for the thermal destruction of tumor cells, providing an additional physical mode of antitumor action. Meanwhile, the temperature-controlled release of a chemotherapeutic agent and hyperthermia itself may synergize and, therefore, provide an enhanced antitumor effect [21,22]. Fourth, MLPSs can be used for MRI-assisted theranostics because iron oxide nanoparticles are known to exhibit a T_2 -shortening effect, resulting in a potent contrasting ability [23].

Different molecules were incorporated into MLPSs for theranostic applications [19]. In the majority of published studies, MLPSs were filled with various anticancer agents such as doxorubicine [22], methotrexate [24], cisplatin [25], and gemcitabine [20]. In addition, there are several reports on the properties and applications of MLPSs containing photosensitizers [26,27] and small interfering RNA [28].

The aim of the present study was to develop MLPSs incorporating an agent with the ability to act both as a photosensitizer and as a fluorophore for optical imaging. In theory, such a construction should improve the functionality of theranostic MLPSs since they would be able to be visualized by two different modalities, MRI and optical imaging. Among several candidates, we selected indocyanine green (ICG) for loading into MLPSs. ICG is an FDA-approved agent for fluorescent angiography [29,30]. In addition, ICG behaves as a photosensitizer and photothermal agent [31]. We therefore aimed to develop a preparation method for ICG-containing MLPSs, followed by a detailed characterization of their physicochemical and magnetic properties. Besides, we were interested in testing the ability of intravenously administered ICG-containing MLPSs to accumulate in the tissue exposed to a constant magnetic field *in vivo*.

2. Materials and methods

2.1. Synthesis of Iron Oxide Magnetic Nanoparticles

All chemicals were purchased from Sigma-Aldrich (St. Louis, MO, USA). Iron oxide magnetic nanoparticles (MNPs) were synthesized by coprecipitation of ferrous and ferric iron ion solutions as described earlier [32]. Briefly, FeSO_4 , $\text{Fe}_2(\text{SO}_4)_3$, and ammonium oxalate were successively dissolved in 250 mL of distilled water in a molar ratio of 1.0:1.0:0.1. Next, a solution of ammonia in water in a ratio of 1:1 was gradually added to the reaction mixture under intensive stirring until the pH had increased to 8.0. The resulting MNPs were washed five times with distilled water, each time followed by magnetic separation using a permanent magnet for 15 min and then redispersed at a concentration of 10 mg/mL, followed by stabilization with sodium citrate (0.1% by weight of magnetite).

2.2. Preparation of ICG-Containing Magnetic Liposomes

Magnetic liposomes were prepared using the thin film hydration approach [33]. Briefly, 75 mg of soy lecithin was dissolved in 15 mL of chloroform, followed by the addition of 10 μL of α -tocopherol acetate (vitamin E). The mixture thus prepared was transferred into a 2000 mL round-bottom flask. The organic solvent was removed by rotary evaporation (RE-5000 Rotary Evaporator, Henan Lanphan Industry Co., Zhengzhou, China) using a vacuum pump (Labport N 810, KNF, Freiburg im Breisgau, Germany) without heating until a thin film was formed. The resulting thin lipid film was dried in a water bath at $35 \pm 5^\circ\text{C}$ until it became transparent. Next, the resulting dry film was hydrated with an aqueous suspension of MNPs containing 0.9% NaCl and ICG at a concentration of 1 mg/mL. The hydration process was continued until the lipid film was completely washed off the walls of the flask. After hydration, the liposomal form was transferred into a polypropylene tube and sonicated with an ultrasonic disperser (UZG13-0.1/22, VNIITVCH, St. Petersburg, Russia) at a frequency of 20 kHz for 25–30 min to obtain unilamellar ICG-containing MLPSs (MLPSICG). The scheme of MLPSICG synthesis is shown in Figure 1. Such an approach resulted in the formation of aqueous magnetoliposomes incorporating both MNPs and ICG in the membrane-enveloped hydrophilic core.

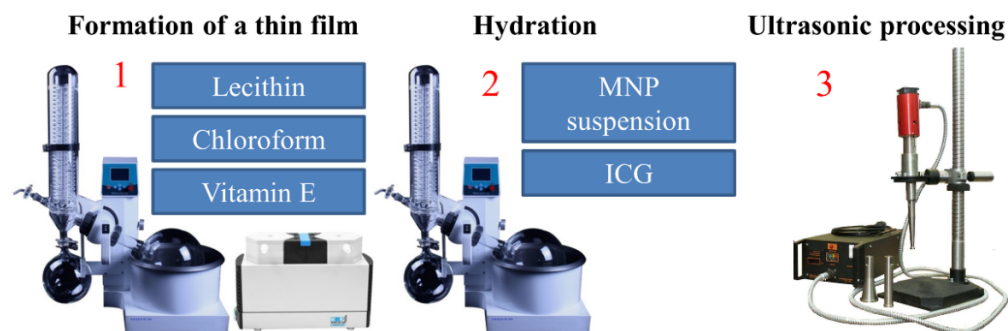


Figure 1. Scheme of the synthesis of aqueous MLPSICG.

2.3. Characterization of MLPSICG

The size distribution and zeta potential of MLPSICG were studied in an aqueous medium by dynamic light scattering (DLS) and electrophoretic light scattering (ELS), respectively, using a Zetasizer Ultra (Malvern Instruments Ltd., Worcestershire, UK).

The static magnetic characteristics of MLPSICG were analyzed in air at a temperature of 25°C using a vibrating sample magnetometer (Lake Shore 7410, Lake Shore Cryotronics Inc., Westerville, OH, USA).

Microphotographs of “large” multilayered liposomes were obtained using a light microscope (Nikon Eclipse E200, Nikon Inc., Tokyo, Japan). MLPSICG size and morphology were assessed by transmission electron microscopy (TEM; JEM-2010, JEOL, Tokyo, Japan).

The content of crystalline phases in the samples was studied on an automatic powder diffractometer (D2 PHASER, Bruker AXS, Billerica, MA, USA) using the following settings:

X-ray tube radiation—CuK α 1+2, tube operation mode—30 kV/10 mA, position-sensitive detector, reflection geometry, Bragg–Brentano focusing scheme, T = 25 °C, air atmosphere. The phases were identified using the PDXL-2 software package (Rigaku, Tokyo, Japan) using the Powder Diffraction File (PDF-2, International Center for Diffraction Data) database. To obtain crystalline samples, MLPs were preliminarily lyophilized by freeze drying (VaCo2, ZirBus, Bad Grund, Harz, Germany) at a temperature of −50 °C and an absolute pressure of 3 Pa. To avoid destruction of liposomes at low temperatures, a cryoprotectant, glucose, was added in an amount of 10 wt % [34].

The Mössbauer measurements were performed in absorption geometry at room temperature on a commercial Mössbauer spectrometer (WISSEL, Ortenberg, Germany). The source of Mössbauer radiation was ^{57}Co in a chromium matrix with an activity of 30 mCi. The parameters of the isomeric chemical shift obtained from processing the experimental spectra are given relative to the standard $\alpha\text{-Fe}$ sample.

2.4. In Vitro MRI Relaxivity Measurements

In vitro MR imaging of the MLPSICG was performed using 9.4 T NMR spectrometer (Bruker Avance III 400 WB, Uster, Switzerland). The MR contrast properties of the MLPs were evaluated using 1.0% agarose matrix phantoms which simulate human soft tissue [35]. The content of MNPs and MLPSICG in the agarose matrix was 0.1 mg/mL. This concentration was chosen after a series of preliminary experiments as giving the optimal color intensity. Layers of pure agarose and agarose with 1 cm-thick samples were alternately poured into a 15 mL polypropylene tube. Although superparamagnetic nanoparticles are almost exclusively T_2 contrast agents, for comparison, longitudinal (T_1) relaxation times were also determined. T_1 - and T_2 -weighted imaging was performed with the following parameters: repetition time = 2500 ms, slice thickness = 1 mm. Echo time was 16.2 and 11.0 ms for T_1 - and T_2 -weighted images, respectively. The resulting data were converted to HDR format and analyzed using the free MRICro software. Staining intensity was assessed using 11 sections for each sample (6 agarose matrix controls, 5 sample sections).

2.5. In Vitro Fluorescent Measurements

Fluorescent properties of MLPSICG were studied using an Ivis Lumina LT fluorescence tomograph (PerkinElmer, Waltham, MA, USA). To register ICG fluorescence, a 745 nm excitation filter was used, and an extraction filter for ICG. The samples studied were: normal saline (background signal), aqueous solution of ICG, aqueous solution of ICG plus albumin in an equivalent amount by weight, aqueous suspension of MLPs, and a suspension of MLPSICG. The measurements were performed in triplicate. Fluorescent signals were digitized using Living Image 4.5.5 software (PerkinElmer Inc., Waltham, MA, USA).

2.6. In Vivo and Ex Vivo Fluorescent Imaging

The study was performed on outbred laboratory male mice of the ICR (CD-1) strain, weighing 25 ± 3 g. Animals were randomized into two groups ($n = 3$ in each group): (1) controls, which were injected with 200 μL of normal saline, and (2) MLPSICG, which were subjected to magnet implantation followed by the administration of MLPSICG. In the latter group, the animals were anesthetized with isoflurane, after which a permanent neodymium magnet was implanted in the muscle tissue of the thigh. In all experiments, a cylindrical axially magnetized Nd-Fe-B alloy magnet, 3 mm in length and 2 mm in diameter, was implanted. The magnet was coated with anticorrosion nickel alloy. A three-dimensional reconstruction showing the location of the magnet and the fluorescence zone was obtained using the multimodal imaging system, IVIS SpectrumCT (PerkinElmer Inc., Waltham, MA, USA). The residual magnetic induction of the permanent magnet was 1.17–1.21 T, the magnetization coercive force >876 kA/m, and the induction coercive force >955 kA/M. The animals in the MLPSICG group were treated with 200 μL of MLPSICG suspension. The introduction of substances in both groups was carried out through the tail vein. The

animals were under inhalation anesthesia with isoflurane throughout the experiment. After intravenous administration of either saline or MLPSICG, the animals were placed in a fluorescent imaging chamber, where inhalation anesthesia with 2% isoflurane and a core body temperature of 37 °C were maintained throughout the experiment. After obtaining images at 5, 10, 15, 20, 25, and 30 min post-injection, the animals were euthanized by an overdose of isoflurane for subsequent isolation and fluorescent image analysis of the heart, lungs, liver, spleen, and kidneys. Analysis of fluorescent signals from selected regions of interest was processed manually using Living Image 4.5.5 software (PerkinElmer Inc., Waltham, MA, USA).

2.7. Statistical Analysis

Statistical processing of the obtained data for relaxivity and fluorescence was performed in GraphPad Prism software using the Mann–Whitney nonparametric U-test. Results were presented as average (mean) \pm standard deviation (SD).

3. Results and Discussion

3.1. Characterization of MLPSICG

Our approach to the synthesis of MLPSICG using thin film hydration is characterized by an appropriate loading efficiency leading to a magnetic moment sufficient for accumulation of nanoparticles in the area of magnetic field application.

According to DLS, the “large” magnetic liposomes obtained at the stage of thin film hydration had an average size of about 1.2 μm (Figure 2a). This result corresponds well with data from direct visualization of MLPSICG using light microscopy (Figure 2c). Subsequent sonication caused the rearrangement of the liposomes with the formation of MLPSICG with an average size of about 170 nm (Figure 2a).

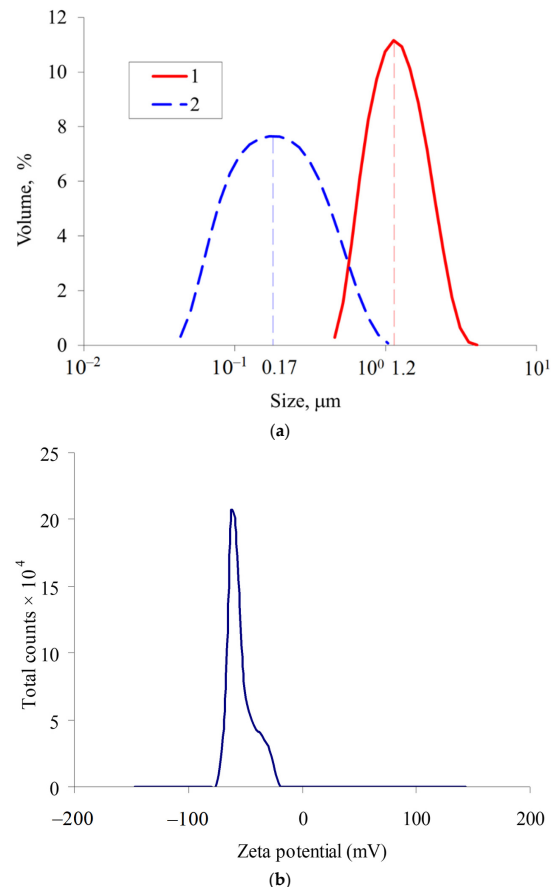


Figure 2. *Cont.*

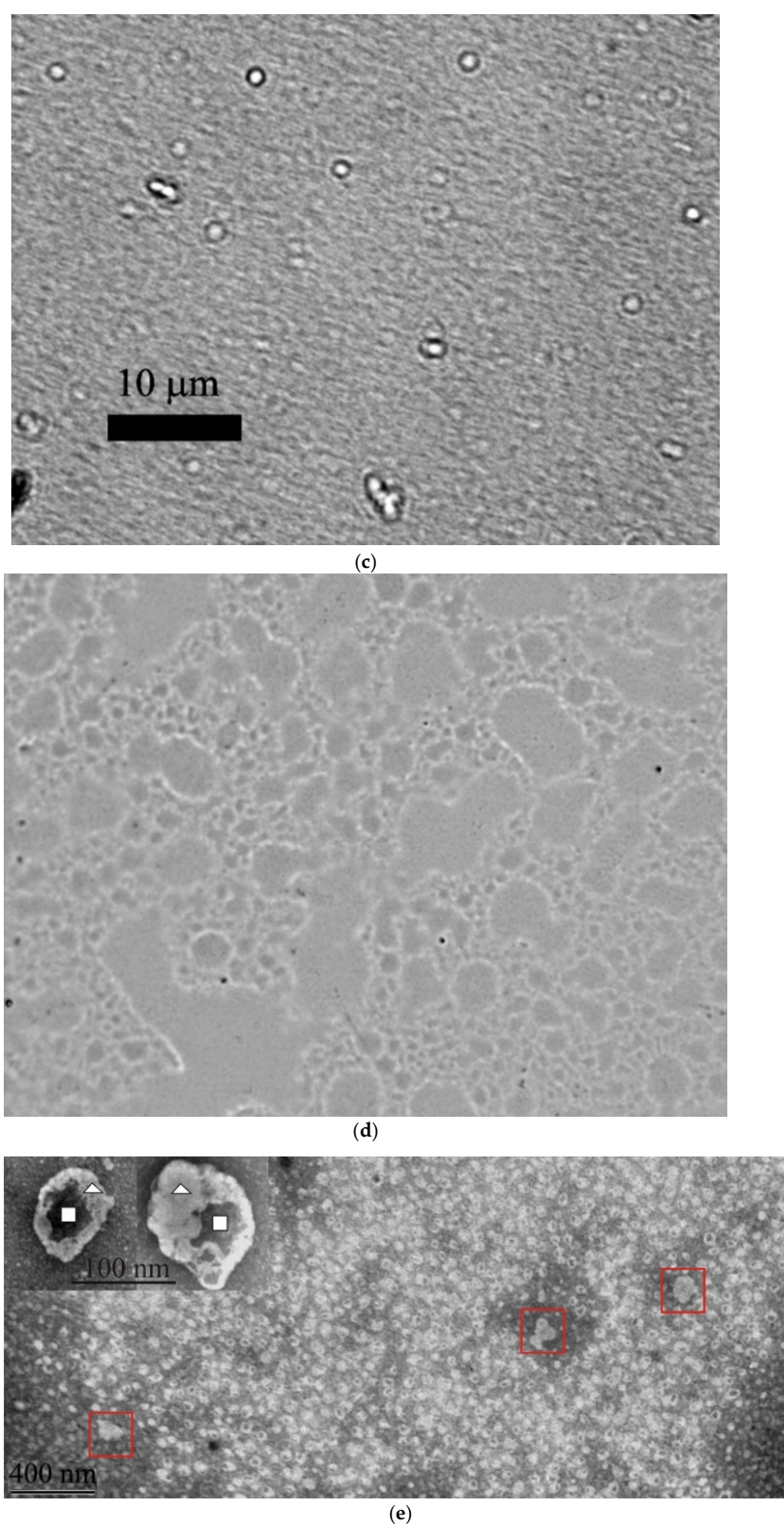


Figure 2. Physicochemical properties of MLPSICG: (a) particle size distribution with dynamic light scattering before (1) and after (2) sonication; (b) zeta potential distribution; (c) light microscopy image of “large” liposomes before sonication; (d) light microscopy microphotograph of dried “large” liposomes; (e) TEM image of MLPSICG. The agglomerated MLPSICG are labeled with red lined squares. The inset shows two enlarged individual liposomes containing magnetite nanoparticle(s) in the core (white squares) and lipid shell (white triangles).

The average zeta potential of the MLPSICG in an aqueous medium as determined by ELS was -51.35 mV (Figure 2b). This value points to good stability of the synthesized colloid. Visual inspection of the colloid demonstrated excellent stability for 6 months at a temperature of $+4$ °C.

Light microscopic examination of the “large” MLPSICG demonstrated their spherical shape and a size of approximately $1\text{ }\mu\text{m}$ (Figure 2c). When dried, the liposomes “burst” leaving only a contour of phospholipids (Figure 2d). This fact led us to the conclusion that in order to obtain TEM images of MLPSICG processed with ultrasound, it is necessary to use a protector. For this purposed, we used glucose. TEM imaging showed the spherical shape of the MLPSICG and yielded their size comparable to that determined with DLS (Figure 2e). It can also be observed that each individual MLPSICG contains magnetite nanoparticle(s) inside. The figure also shows agglomerates consisting of several adherent liposomes. This is due to the fact that a certain time elapsed from the moment of synthesis to the analysis of TEM images, during which some of the liposomes agglomerated.

The study of the magnetization reversal curves of the MLPSICG lyophilizate made it possible to determine a saturation magnetization equal to 5.36 emu/g (Figure 3a). This value for magnetic fluids is $10\text{--}12$ emu/g [36], which makes it possible to predict the accumulation of MLPSICG in the area of magnetic field action. The plot of the dependence of the magnetic moment on the field strength in the zone of low field values shows a coercive force equal to 40 oersteds (Figure 3b). According to Bertotti (1998) [37], liposomes are soft magnetic materials with a relatively low coercive force. After the magnetic liposomes burst due to unprotected drying, whatever properties are measured are not those of liposomes, but rather the properties of the fragments and spilled contents.

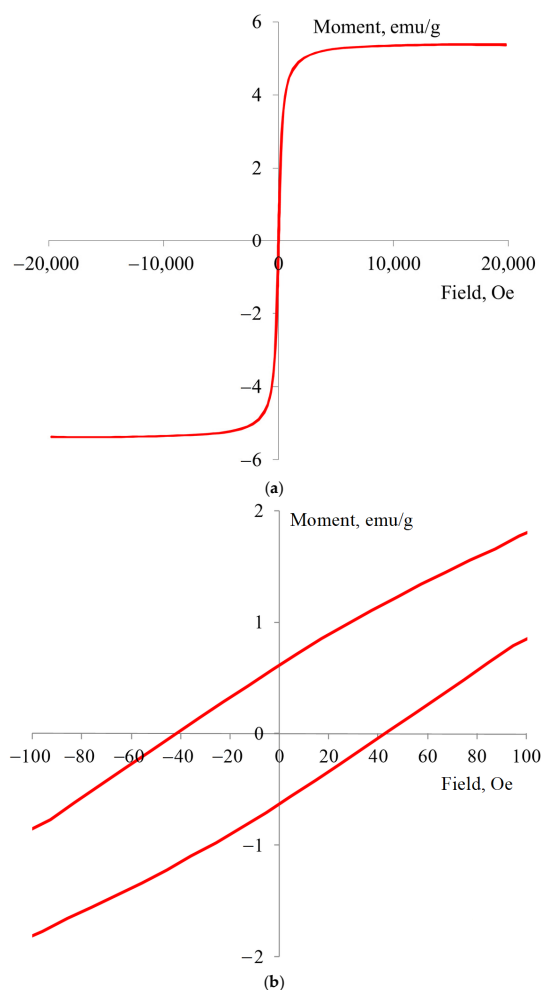


Figure 3. Cont.

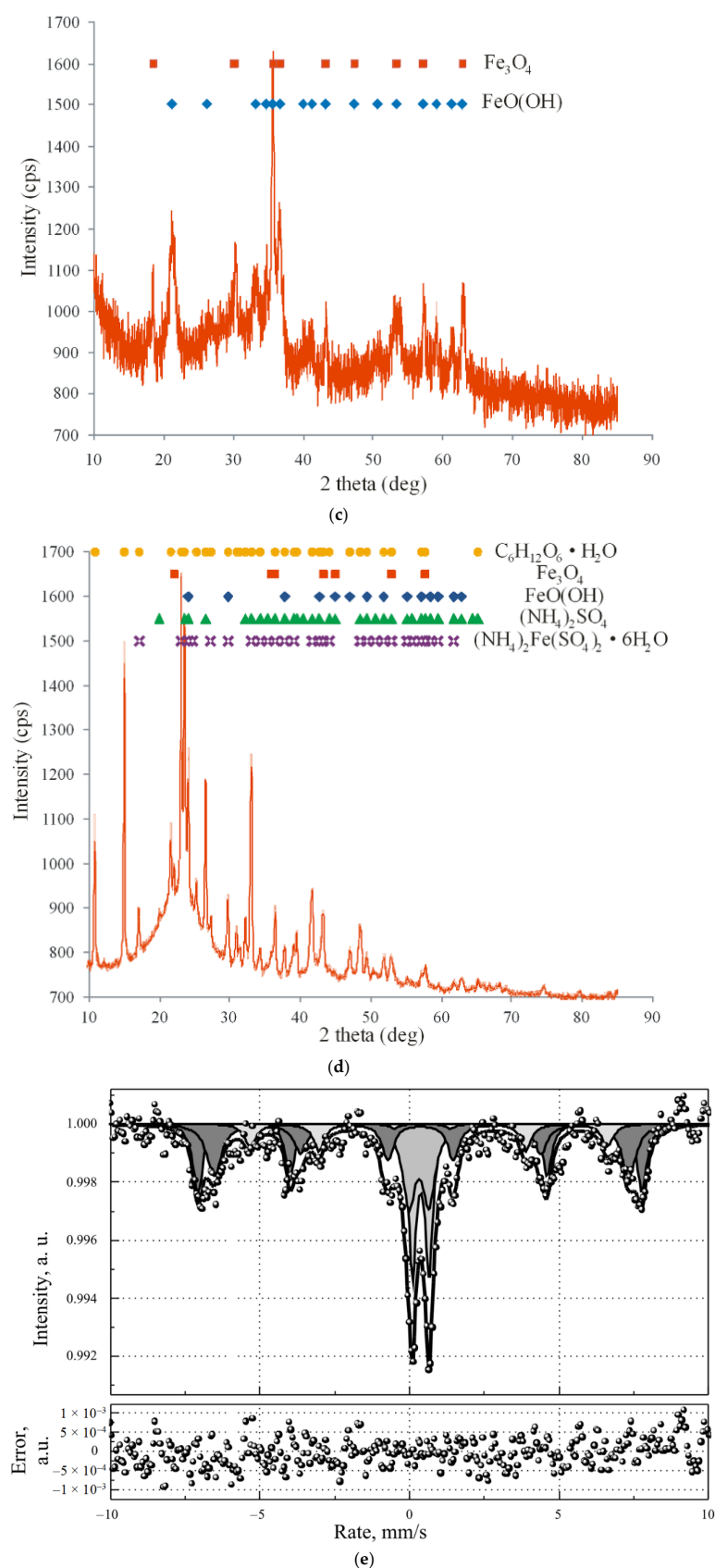


Figure 3. Magnetic properties and composition of MLPSICG: (a,b) magnetization reversal curves of MLPSICG; (a) full scale; (b) in the zone of small fields; (c) X-ray phase analysis of samples of MNP; (d) X-ray phase analysis of MLPSICG; (e) Mössbauer spectra of a sample of MLPSICG.

The X-ray diffraction pattern of the MLPSICG shows the presence of magnetite [Fe_3O_4] and goethite [$\text{FeO}(\text{OH})$], as well as the initial magnetic nanoparticles that were used in the synthesis of MLPSICG (Figure 3c). At the same time, the X-ray pattern also contains a crystalline phase of glucose, which was used as a cryoprotectant for sample lyophilization, and the more complex compounds of maskagnit [$(\text{NH}_4)_2\text{SO}_4$] and morite [$(\text{NH}_4)_2\text{Fe}(\text{SO}_4)_2 \times 6\text{H}_2\text{O}$], which are by-products from the synthesis (Figure 3d). Among all the phases detected, only magnetite is magnetic. These by-products were not removed due to the difficulty of their removal when combined with phospholipids compared with when they are combined with pure magnetite nanoparticle.

To quantitatively determine the phases of iron compounds in the MLPSICG, Mössbauer spectra were obtained (Figure 3e). The results of spectral analysis and decomposition into subspectra are shown in Table 1.

Table 1. Results of processing MLPSICG Mössbauer spectra.

N	Substance	Chem. Shift mm/s	Quadrupole Splitting mm/s	Ultrafine Magnetic Field, Tl	Proportion of Iron Atoms %
1	Fe^{+3} 1st state	0.37 ± 0.02	0.56 ± 0.05	—	20.3
2	Fe^{+3} 2nd state	0.31 ± 0.07	0.67 ± 0.12	—	17.3
3	Fe_3O_4 (A)	0.32 ± 0.02	0.04 ± 0.04	46.108 ± 0.166	23.4
4	Fe_3O_4 (B)	0.38 ± 0.03	0.03 ± 0.06	43.068 ± 0.307	28.0
5	$\alpha\text{-FeOOH}$	0.53 ± 0.05	0.21 ± 0.11	37.099 ± 0.434	11.0

In the samples under study, iron was found in five nonequivalent environments. The first two states were non-magnetic, with the oxidation state Fe^{+3} . Unfortunately, it was not possible to identify these states more accurately. The percentage of iron within these two states is 37.6%. The third and fourth states of iron were magnetite, with reduced values of the hyperfine magnetic field. The proportion of iron in the magnetite state is 61.3%. The fifth state corresponds in parameters to iron hydroxide $\alpha\text{-FeOOH}$. The proportion of iron in $\alpha\text{-FeOOH}$ is equal to 11%.

In general, the amount of magnetite in the samples is quite high. In this case, the relatively low saturation magnetization of the MLPSICG is explained by the moderate extent of MNP incorporation into the MLPSICG.

3.2. Magnetic Resonance Contrast Properties of MLPSICG

It was long recognized that iron oxide nanoparticles possess superparamagnetic properties that allow them to be used as T_2 contrast agents for MRI. MLPSICG could also be potentially used for MR imaging owing to the presence of MNPs in their core. In order to test the MR-contrasting properties of MLPSICG, we determined their T_1 and T_2 values versus the intact agarose matrix, as well as the transverse relaxivity r_2 (Figure 4). The average T_1 time for a 1% agarose gel was 2672 ± 35 ms (Figure 4a), which is significantly greater than the analogous value for biological tissue. Presumably, this is due to the fact that the gel contains 99% water, for which this parameter is equal to 4500 ms. The T_2 value for the agarose gel was 53.0 ± 0.7 ms (Figure 4b), which corresponds well with the value typical of soft tissues. For example, the T_2 time was estimated at 22.40 ± 5.61 ms and 36.36 ± 8.77 ms for normal glandular tissue and fat, respectively [38]. Our results show that MLPSICG had no effect on T_1 but significantly decreased the T_2 value, i.e., they demonstrate the activity of a negative contrast agent. These data are in good agreement with available evidence on MLPSs [23]. The obtained value of r_2 for MLPSICG is $43.8 \text{ mM}^{-1} \times \text{s}^{-1}$, which is within the range reported in the literature for MLPSs, that is, from 60 to $323 \text{ mM}^{-1} \times \text{s}^{-1}$ [24,39–41]. Multiple factors are known to influence the value of the transverse relaxivity of MNPs [23]. First, most studies demonstrated an increase in r_2 after the encapsulation of MNPs into the lipid membranes. For example, Carvallo et al. showed that envelopment of 10-nm MNPs with egg phosphatidylcholine, cholesterol, and N-[carbonyl-methoxy(polyethylene

glycol)-2000]-1,2-distearoyl-sn-glycero-3-phosphoethanolamine resulted in an increase in r_2 from 47.4 to 210 $\text{mM}^{-1} \times \text{s}^{-1}$ [42]. Second, the r_2 value is affected by the composition of the lipid envelope. It was shown that the presence of cholesterol in the membrane is associated with decreased r_2 . Although cholesterol decreases the fluidity of the membrane, its addition might be useful because it increases the in vivo stability of liposomes. The preparation of liposomal membrane from unsaturated lipid acyl chains, as well as the inclusion of a negatively charged lipid into the bilayer, appeared to result in a markedly increased negative contrast [43]. Finally, PEGylation of the MLPS surface is known to result in increased hydration of the liposomes and, thus, an elevated r_2 [44]. Taking into account that PEGylation increases the circulatory half-life of liposomes, such a modification is considered especially beneficial for theranostic applications. However, recent evidence suggested a certain extent of PEG immunogenicity associated with the formation of anti-PEG antibodies, resulting in the enhanced clearance of PEGylated liposomes from the circulation [45]. One promising approach to circumvent this problem might include the use of biomimetic MNP-containing nanostructures, such as encapsulation in red blood cell membrane [46]. In conclusion, the measurements of MRI signals confirmed the feasibility of using MLPSICG as contrast agents for MRI, although this possibility was not validated in the in vivo settings.

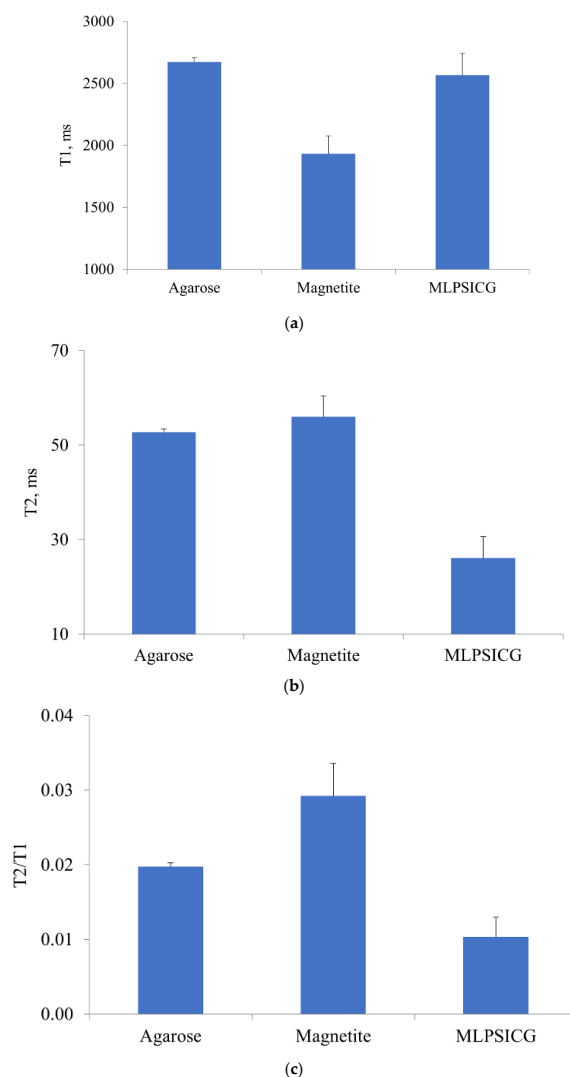


Figure 4. Magnetic resonance contrast properties of samples. T_1 and T_2 values, as well as the T_2/T_1 ratio, were determined using NMR spectrometry in pure 1.0% agarose matrix blocks, MNP-containing blocks, and MLPSICG-containing blocks: (a) T_1 ; (b) T_2 ; (c) T_2/T_1 ratio.

3.3. In Vitro, Ex Vivo, and In Vivo Fluorescent Properties of MLPSICG

To explore the possibility of using MLPSICG for fluorescence imaging, preliminary in vitro studies were performed (Figure 5a). The strongest fluorescent signal was registered in the ICG + human albumin sample, which may be attributed to the previously described augmentation of fluorescent properties of ICG by albumin [47]. The latter effect is also relevant to the in vivo fluorescent imaging with ICG. Supporting these findings, the ICG sample without albumin demonstrated a lower fluorescence intensity than ICG + albumin. MLPSICG were characterized by slightly lower fluorescence levels compared with the free ICG solution, probably due to the shielding effect of the lipid membrane and the absorption of secondary radiation by MNPs. The MNP suspension and blank samples produced near-zero fluorescence. In this pilot experiment, MLPSICG demonstrated potent fluorescent properties, which enabled us to draw a conclusion about their suitability for in vivo fluorescent imaging.

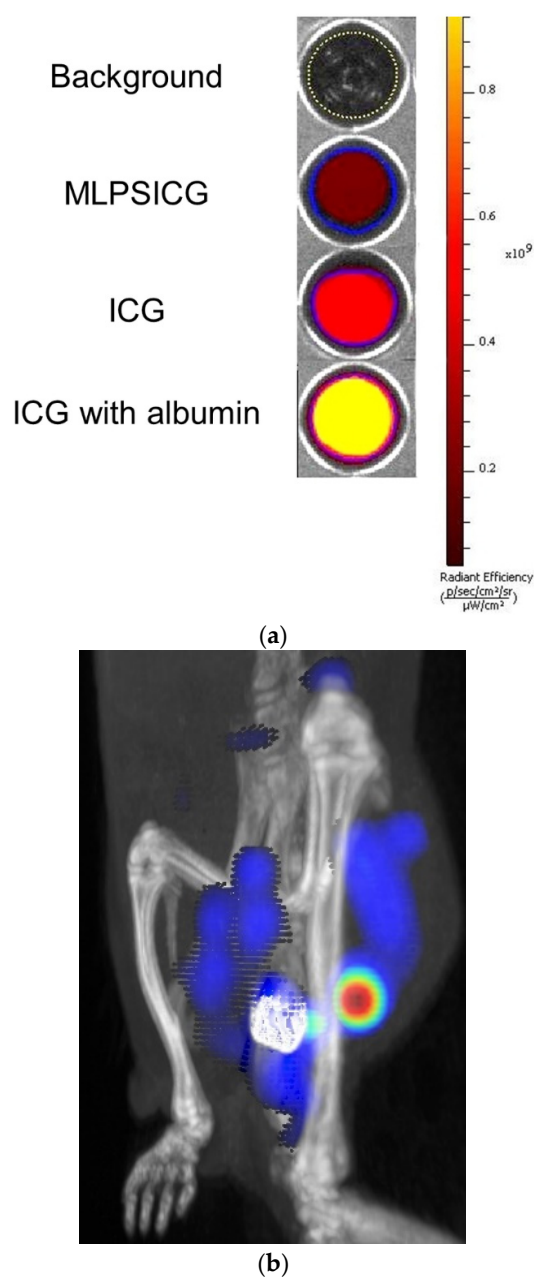


Figure 5. Cont.

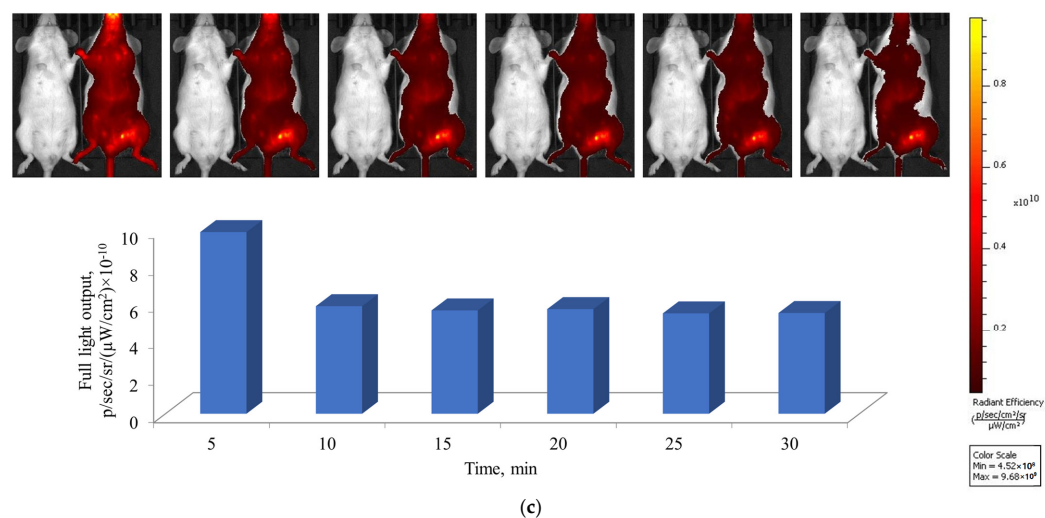


Figure 5. Fluorescent properties of magnetic liposomes with a fluorophore: (a) in vitro fluorescence study; (b) 3D reconstruction of the area of magnet implantation and the fluorescence zone; (c) distribution of fluorescence in time in the area of action of the magnetic field and changes in fluorescence intensity in the zone of action of the magnetic field over the period of 30 min after intravenous administration. The order of images corresponds to 5, 10, 15, 20, 25, and 30 min post-injection.

To monitor the accumulation of MLPSICG in the zone of action of the magnetic field, a permanent magnet was implanted in the soft tissues of the hip, as shown in Figure 5b. After intravenous administration of MLPSICG, their accumulation was observed in the zone of action of the magnetic field of a permanent magnet (Figure 5c). The maximal level of fluorescence was observed 5 min after injection. Starting from the 10th min post-injection, the value of fluorescence remained at a relatively stable level. This might be attributed to the process of rapid MLPSICG destruction taking place during the first 5–10 min after administration and accumulation. It is conceivable that the remaining part of intact MLPSICG accumulated in the area of interest provides a stable level of fluorescence in a prolonged manner, until the process of MLPSICG stepwise biodegradation starts.

MLPSICG biodistribution was studied at 30 min after their intravenous administration in the same animals by means of registering the NIR fluorescence intensity in the main organs (Table 2, Figure 6). Compared with controls, the greatest level of fluorescence was observed in the liver, which is indicative of the pronounced liver accumulation of MLPSICG. This is consistent with previous studies on the biodistribution of lipid-based ICG-incorporating nanoparticles [48,49]. The liver is considered to be the main organ of the reticuloendothelial system, with the Kupffer cells being responsible for the recognition of opsonized foreign particles and their phagocytosis [50]. A moderate but significant accumulation of MLPSICG was also observed in the lung and spleen which represent secondary organs of the reticuloendothelial system owing to the activity of alveolar and splenic macrophages, respectively. The significant elevation of fluorescence intensity in the kidney might point to the renal excretion pathway of MLPSICG. There was no accumulation of MLPSICG in the heart, possibly due to the low number of cardiac macrophages and the strong barrier function of cardiac capillaries.

Table 2. Numerical characteristics of the distribution of fluorescence in organs.

Organs	Full Light Output, $p/sec/sr/(\mu W/cm^2) \times 10^{-10}$		
	Control	MLPSICG	Difference
Heart	0.02	0.23	0.21
Lungs	0.10	1.53	1.43
Liver	0.39	28.90	28.51
Spleen	0.04	2.10	2.06
Kidneys	0.03	1.44	1.41

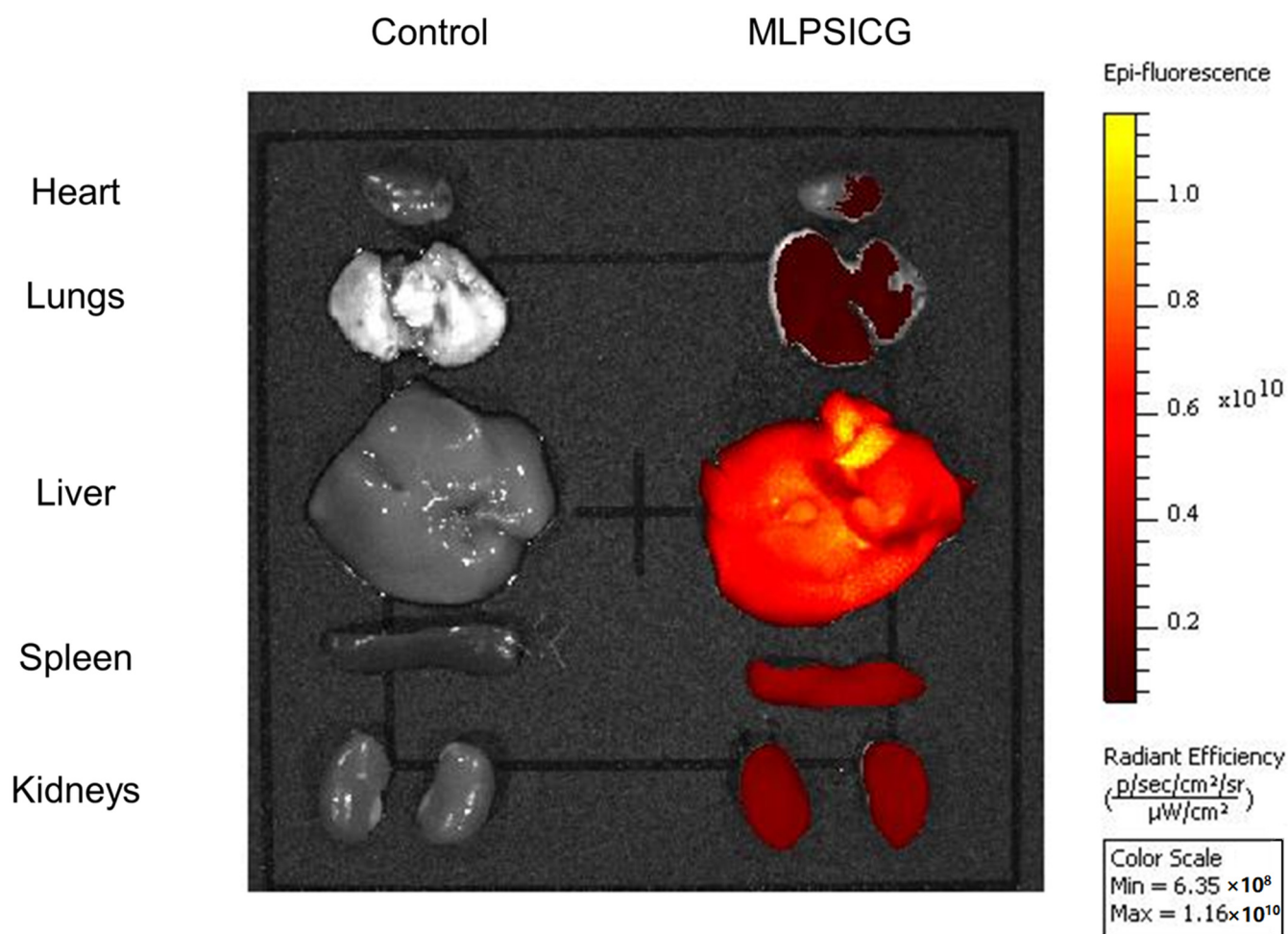


Figure 6. Representative samples of ex vivo organs demonstrating biodistribution of MLPSICG. ICR mice weighing 25 ± 3 g received an injection of 200 μ L of MLPSICG suspension in the tail vein, while controls received the equivalent volume of normal saline. The animals were euthanized at 30 min post-injection, followed by isolation and fluorescent image analysis of the heart, lungs, liver, spleen, and kidneys.

At present, considerable efforts are directed at examining the properties of various ICG-incorporating nanoparticles, such as liposomes [51], polymer-based nanoparticles [52], mesoporous silica nanoparticles [53], iron oxide [54], and calcium phosphate nanoparticles [55]. In general, ICG incorporation into nanoparticles results in minimization of such drawbacks of free ICG as concentration-dependent aggregation and self-quenching [56], a short circulatory half-life, limited photostability, and nonspecific binding to protein targets [57]. Some data on the beneficial effects associated with ICG incorporation into liposomes are available. For instance, Suganami et al. demonstrated improved imaging capacity of 191-nm ICG-containing N-(carbonyl-methoxypolyethylene glycol 5000)-1,2-distearoyl-sn-glycero-3-phosphoethanolamine-covered liposomes in the rat model of a brain tumor compared with aqueous ICG used in the equivalent dose [51]. Using a mouse model of colon adenocarcinoma, Beziere et al. reported better accumulation of liposomal ICG within the tumor, as well as a greater photoacoustic signal generated by the liposomal versus free ICG [48]. It was shown that liposomal encapsulation of ICG resulted not only in the improved imaging characteristics of the molecule, but also in the optimization of its therapeutic effectiveness, including photodynamic, photothermal, and photoacoustic activity. It is well known that ICG demonstrates strong absorbance in the near infrared (NIR) area and exhibits both photodynamic and photothermal effects after irradiation with an 808-nm laser [58]. ICG-containing, folic acid-decorated liposomes were used for

photothermal tumor therapy combined with NIR imaging [59]. In this work, systemic administration of ICG-incorporating liposomes resulted in a pronounced antitumor effect in a murine xenograft model of breast cancer. Most notable are the studies on dual-mode therapy using ICG-containing liposomes. For example, Yan et al. successfully used 115-nm ICG liposomes functionalized with RGD peptide for combined photodynamic and photothermal therapy of breast cancer in mice [60]. Using a xenograft murine model of breast adenocarcinoma, Zhao et al. showed that intratumor administration of PEGylated liposomes co-encapsulating doxorubicin and ICG resulted in the synergistic photothermal efficacy of ICG and the chemotherapeutic efficacy of doxorubicin [61]. Thus, ICG encapsulation in the liposomes improved both the imaging and therapeutic parameters in this multifunctional molecule.

Although liposomal ICG was studied in several above-mentioned works, we failed to identify those studies exploring the properties of ICG-incorporating magnetoliposomes. One study focused on MNPs containing ICG in their layer-by-layer casein coating. However, in that study, the nanoparticles were administered orally, demonstrating their resistance to a highly acidic gastric environment with subsequent accumulation in the intestine [54]. The theranostic platform developed in the present study resembles the above benefits of liposomal ICG but, owing to the presence of MNPs, it has potential additional functional properties, including magnetic field-guided active targeting, visualization with MRI, and the hyperthermic destruction of pathological cells after heating with an alternating magnetic field.

One can anticipate that the MLPSICG synthesized in the present study might be used for theranostic applications, not only in the field of oncology but also in other areas of biomedicine. For example, targeted delivery of cardioprotective drugs in the area of myocardial ischemia–reperfusion resulting in greater infarct-size limitation, while reducing unwanted side effects [62]. It was shown in mice that gadolinium-doped, fluorescent 100-nm liposomes selectively accumulated in the area of myocardial ischemia–reperfusion 24 h after their administration, which was verified using optical imaging and MRI [63]. In another study, paramagnetic liposomes and micelles were found to be accumulated in the infarcted area of the heart after permanent coronary occlusion; this enabled the authors to conclude that the use of contrasting liposomes may ensure targeted delivery of anti-ischemic and antiremodeling drugs directly to the injured myocardium [64]. In some cardiovascular disorders, therapeutic targeting aims not simply to salvage injured tissue, but rather to inactivate the cells demonstrating pathological activity. The latter scenario is observed in the case of targeted ablation of cardiac ganglionated plexi, which enhanced activity involved in the initiation and maintenance of atrial fibrillation. One study demonstrated that external magnetic field-guided accumulation of MNPs with a calcium chloride payload in the ganglionated plexi resulted in the inhibition of pathological neuronal activity secondary to calcium-mediated neurotoxicity [65]. It follows, therefore, that magnetoliposomes containing ICG and/or other active molecules represent a promising theranostic nanoplatform for various biomedical applications.

4. Conclusions

Using the thin film hydration method, 170-nm aqueous liposomes containing magnetic nanoparticles and indocyanine green were synthesized, followed by a detailed characterization of their physicochemical properties. It was shown that ICG-containing magnetoliposomes (MLPSICG) possess the properties of T₂ contrast for MRI. In addition, MLPSICG were clearly visualized using near infrared fluorescent imaging, which was demonstrated in *in vivo* experiments showing the accumulation of MLPSICG in the zone of the magnetic field distribution produced by a constant magnet previously implanted in the tissue. Although not directly tested in the present study, potential therapeutic applications of MLPSICG include magnetic hyperthermia, as well as the photodynamic, photothermal, and photoacoustic effects of ICG. Future studies are needed to address such issues as the ability of MLPSICG to accumulate in the tumor tissue *in vivo*, and the presence of antitumor

effects of MLPSICG based on the magnetic hyperthermia and photodynamic/photothermal effects of ICG. Taking into account the fact that liposomes, iron oxide nanoparticles, and ICG are all FDA-approved agents, it is highly likely the MLPSICG could be successfully translated to clinical practice.

Author Contributions: Project administration, conceptualization, methodology, D.V.K. and M.M.G.; writing—review and editing, I.V.A.; investigation, resources, writing—original draft preparation, G.A.S., A.I.N. and M.S.I.; Mössbauer research, V.G.S. All authors have read and agreed to the published version of the manuscript.

Funding: The study has been supported by the grant from the Ministry of Science and Higher Education of the Russian Federation (agreement 075-15-2020-800).

Institutional Review Board Statement: The experiments were performed in compliance with the principles of human treatment of animals, regulated by the requirements of the European Convention (Strasbourg, 1986) for the housing, feeding, and care of experimental animals and in accordance with the “Guide for the Care and Use of Laboratory Animals” (National Institute of Health publication No. 85-23, U.S.A.) and “Guideline for experimental (preclinical) studying of new pharmacological substances.” All procedures involving animal use in the study were reviewed and approved by the Commission for Control of the Housing and Use of Laboratory Animals of the Almazov National Medical Research Centre and were deemed in compliance with the ethical requirements for the handling of laboratory animals.

Informed Consent Statement: Not applicable.

Data Availability Statement: Not applicable.

Acknowledgments: The work was carried out using the equipment in the following Resource Centers, “Optical and Laser Methods for Studying Substances”, “X-ray Diffraction Research Methods”, and “Innovative Technologies of Composite Nanomaterials” at St. Petersburg State University.

Conflicts of Interest: The authors declare no conflict of interest.

References

- Freeman, A.I.; Mayhew, E. Targeted drug delivery. *Cancer* **1986**, *58*, 573–583. [\[CrossRef\]](#)
- Douglas, S.J.; Davis, S.S.; Illum, L. Nanoparticles in drug delivery. *Crit. Rev. Ther. Drug Carrier Syst.* **1987**, *3*, 233–261. [\[PubMed\]](#)
- Kwon, I.K.; Lee, S.C.; Han, B.; Park, K. Analysis on the current status of targeted drug delivery to tumors. *J. Control. Release* **2012**, *164*, 108–114. [\[CrossRef\]](#)
- Bhatia, R.; Sharma, A.; Narang, R.K.; Rawal, R.K. Recent Nanocarrier Approaches for Targeted Drug Delivery in Cancer Therapy. *Curr. Mol. Pharmacol.* **2021**, *14*, 350–366. [\[CrossRef\]](#) [\[PubMed\]](#)
- Jiang, Y.; Lin, W.; Zhu, L. Targeted Drug Delivery for the Treatment of Blood Cancers. *Molecules* **2022**, *27*, 1310. [\[CrossRef\]](#)
- Matsumura, Y.; Maeda, H. A new concept for macromolecular therapeutics in cancer chemotherapy: Mechanism of tumortropic accumulation of proteins and the antitumor agent smancs. *Cancer Res.* **1986**, *46*, 6387–6392. [\[PubMed\]](#)
- Ahmad, A.; Khan, F.; Mishra, R.K.; Khan, R. Precision Cancer Nanotherapy: Evolving Role of Multifunctional Nanoparticles for Cancer Active Targeting. *J. Med. Chem.* **2019**, *62*, 10475–10496. [\[CrossRef\]](#) [\[PubMed\]](#)
- Galagudza, M.; Korolev, D.; Postnov, V.; Naumisheva, E.; Grigorova, Y.; Uskov, I.; Shlyakhto, E. Passive targeting of ischemic-reperfused myocardium with adenosine-loaded silica nanoparticles. *Int. J. Nanomed.* **2012**, *7*, 1671–1678. [\[CrossRef\]](#) [\[PubMed\]](#)
- de Steenwinkel, J.E.M.; van Vianen, W.; ten Kate, M.T.; Verbrugh, H.A.; van Agtmael, M.A.; Schiffelers, R.M.; Bakker-Woudenberg, I.A.J.M. Targeted drug delivery to enhance efficacy and shorten treatment duration in disseminated *Mycobacterium avium* infection in mice. *J. Antimicrob. Chemother.* **2007**, *60*, 1064–1073. [\[CrossRef\]](#)
- Nasr, S.H.; Rashidijahanabad, Z.; Ramadan, S.; Kauffman, N.; Parameswaran, N.; Zinn, K.R.; Qian, C.; Arora, R.; Agnew, D.; Huang, X. Effective atherosclerotic plaque inflammation inhibition with targeted drug delivery by hyaluronan conjugated atorvastatin nanoparticles. *Nanoscale* **2020**, *12*, 9541–9556. [\[CrossRef\]](#)
- Lammers, T.; Aime, S.; Hennink, W.E.; Storm, G.; Kiessling, F. Theranostic nanomedicine. *Acc. Chem. Res.* **2011**, *44*, 1029–1038. [\[CrossRef\]](#)
- Dasgupta, A.; Biancacci, I.; Kiessling, F.; Lammers, T. Imaging-assisted anticancer nanotherapy. *Theranostics* **2020**, *10*, 956–967. [\[CrossRef\]](#) [\[PubMed\]](#)
- Chen, S.; Hao, X.; Liang, X.; Zhang, Q.; Zhang, C.; Zhou, G.; Shen, S.; Jia, G.; Zhang, J. Inorganic Nanomaterials as Carriers for Drug Delivery. *J. Biomed. Nanotechnol.* **2016**, *12*, 1–27. [\[CrossRef\]](#) [\[PubMed\]](#)
- Mitchell, M.J.; Billingsley, M.M.; Haley, R.M.; Wechsler, M.E.; Peppas, N.A.; Langer, R. Engineering precision nanoparticles for drug delivery. *Nat. Rev. Drug Discov.* **2021**, *20*, 101–124. [\[CrossRef\]](#) [\[PubMed\]](#)

15. Nsairat, H.; Khater, D.; Sayed, U.; Odeh, F.; Bawab, A.A.; Alshaer, W. Liposomes: Structure, composition, types, and clinical applications. *Heliyon* **2022**, *8*, e09394. [[CrossRef](#)] [[PubMed](#)]
16. Allen, T.M.; Cullis, P.R. Liposomal drug delivery systems: From concept to clinical applications. *Adv. Drug Deliv. Rev.* **2013**, *65*, 36–48. [[CrossRef](#)] [[PubMed](#)]
17. Lamichhane, N.; Udayakumar, T.S.; D'Souza, W.D.; Simone, C.B., II; Raghavan, S.R.; Polf, J.; Mahmood, J. Liposomes: Clinical Applications and Potential for Image-Guided Drug Delivery. *Molecules* **2018**, *23*, 288. [[CrossRef](#)]
18. Anilkumar, T.S.; Shalumon, K.T.; Chen, J.P. Applications of Magnetic Liposomes in Cancer Therapies. *Curr. Pharm. Des.* **2019**, *25*, 1490–1504. [[CrossRef](#)]
19. Veloso, S.R.S.; Andrade, R.G.D.; Castanheira, E.M.S. Magnetoliposomes: Recent advances in the field of controlled drug delivery. *Expert Opin. Drug Deliv.* **2021**, *18*, 1323–1334. [[CrossRef](#)]
20. Ferreira, R.V.; da Mata Martins, T.M.; Goes, A.M.; Fabris, J.D.; Cavalcante, L.C.D.; Outon, L.E.F.; Domingues, R.Z. Thermosensitive gemcitabine-magnetoliposomes for combined hyperthermia and chemotherapy. *Nanotechnology* **2016**, *27*, 085105. [[CrossRef](#)] [[PubMed](#)]
21. Ribeiro, R.F.L.; Ferreira, R.V.; Pedersoli, D.C.; Paiva, P.R.P.; da Silva Cunha, P.; Goes, A.M.; Domingues, R.Z. Cytotoxic effect of thermosensitive magnetoliposomes loaded with gemcitabine and paclitaxel on human primary breast cancer cells (MGSO-3 line). *J. Nanopart. Res.* **2020**, *22*, 172. [[CrossRef](#)]
22. Chen, B.; Zhang, R.; Wu, H.; Li, M.; Zhou, G.; Ji, M. Thermoresponsive magnetoliposome encapsulating doxorubicin and high performance Ferumoxytol for effective tumor synergistic therapy in vitro. *J. Drug Deliv. Sci. Technol.* **2020**, *57*, 101677. [[CrossRef](#)]
23. Kostevšek, N. A Review on the Optimal Design of Magnetic Nanoparticle-Based T₂ MRI Contrast Agents. *Magnetochemistry* **2020**, *6*, 11. [[CrossRef](#)]
24. Guo, Y.; Zhang, Y.; Ma, J.; Li, Q.; Li, Y.; Zhou, X.; Zhao, D.; Song, H.; Chen, Q.; Zhu, X. Light/magnetic hyperthermia triggered drug released from multi-functional thermo-sensitive magnetoliposomes for precise cancer synergetic theranostics. *J. Control. Release* **2018**, *272*, 145–158. [[CrossRef](#)]
25. Toro-Cordova, A.; Flores-Cruz, M.; Santoyo-Salazar, J.; Carrillo-Nava, E.; Jurado, R.; Figueroa-Rodriguez, P.A.; Lopez-Sanchez, P.; Medina, L.A.; Garcia-Lopez, P. Liposomes Loaded with Cisplatin and Magnetic Nanoparticles: Physicochemical Characterization, Pharmacokinetics, and In-Vitro Efficacy. *Molecules* **2018**, *23*, 2272. [[CrossRef](#)] [[PubMed](#)]
26. Bolfarini, G.C.; Siqueira-Moura, M.P.; Demets, G.J.F.; Morais, P.C.; Tedesco, A.C. In vitro evaluation of combined hyperthermia and photodynamic effects using magnetoliposomes loaded with cucurbituril zinc phthalocyanine complex on melanoma. *J. Photochem. Photobiol. B* **2012**, *115*, 1–4. [[CrossRef](#)]
27. Di Corato, R.; Béalle, G.; Kolosnjaj-Tabi, J.; Espinosa, A.; Clément, O.; Silva, A.K.A.; Ménager, C.; Wilhelm, C. Combining magnetic hyperthermia and photodynamic therapy for tumor ablation with photoresponsive magnetic liposomes. *ACS Nano* **2015**, *9*, 2904–2916. [[CrossRef](#)] [[PubMed](#)]
28. Yang, Y.; Xie, X.; Xu, X.; Xia, X.; Wang, H.; Li, L.; Dong, W.; Ma, P.; Yang, Y.; Liu, Y.; et al. Thermal and magnetic dual-responsive liposomes with a cell-penetrating peptide-siRNA conjugate for enhanced and targeted cancer therapy. *Colloids Surf. B Biointerfaces* **2016**, *146*, 607–615. [[CrossRef](#)] [[PubMed](#)]
29. Venkatesh, R.; Reddy, N.G.; Prabhu, V.; Rishi, P.; Pereira, A.; Bhatt, A.; Yadav, N.K.; Chhablani, J. Indocyanine green angiography imaging findings in artery occlusions. *Eur. J. Ophthalmol.* **2022**, *32*, 2395–2403. [[CrossRef](#)] [[PubMed](#)]
30. Zhang, W.; Che, X. Effect of indocyanine green fluorescence angiography on preventing anastomotic leakage after colorectal surgery: A meta-analysis. *Surg. Today* **2021**, *51*, 1415–1428. [[CrossRef](#)]
31. Kuo, W.S.; Chang, Y.T.; Cho, K.C.; Chiu, K.C.; Lien, C.H.; Yeh, C.S.; Chen, S.J. Gold nanomaterials conjugated with indocyanine green for dual-modality photodynamic and photothermal therapy. *Biomaterials* **2012**, *33*, 3270–3278. [[CrossRef](#)] [[PubMed](#)]
32. Toropova, Y.G.; Golovkin, A.S.; Malashicheva, A.B.; Korolev, D.V.; Gorshkov, A.N.; Gareev, K.G.; Afonin, M.V.; Galagudza, M.M. In vitro toxicity of Fe_mO_n, Fe_mO_n-SiO₂ composite, and SiO₂-Fe_mO_n core-shell magnetic nanoparticles. *Int. J. Nanomedicine* **2017**, *12*, 593–603. [[CrossRef](#)] [[PubMed](#)]
33. Ghazanfari, M.R.; Jaafari, M.R.; Shams, S.F.; Kashefi, M. Design and fabrication of multifunctional temperature-sensitive magnetoliposomal nanostructures. *Mater. Today Commun.* **2017**, *13*, 102–111. [[CrossRef](#)]
34. Dmitrieva, M.V.; Lugen, B.; Polozkova, A.P.; Orlova, O.L.; Krasnyuk, I.I.; Krasnyuk, I.I., Jr. Selection of a cryoprotector for production a lyophilized liposomal dosage form of the indolocarbazole derivative LHS-1269. *Russ. J. Biother.* **2021**, *20*, 74–79. [[CrossRef](#)]
35. Zheltova, V.; Vlasova, A.; Bobrysheva, N.; Abdullin, I.; Semenov, V.; Osmolowsky, M.; Voznesenskiy, M.; Osmolovskaya, O. Fe₃O₄@HAp core-shell nanoparticles as MRI contrast agent: Synthesis, characterization and theoretical and experimental study of shell impact on magnetic properties. *Appl. Surf. Sci.* **2020**, *531*, 147352. [[CrossRef](#)]
36. Charles, S.W. Magnetic fluids (ferrofluids). In *Magnetic Properties of Fine Particles*, 1st ed.; Dormann, J.L., Fiorani, D., Eds.; North-Holland: Amsterdam, The Netherlands, 1992; pp. 267–276. ISBN 9780444597410.
37. Bertotti, G. *Hysteresis in Magnetism: For Physicists, Materials Scientists, and Engineers*, 1st ed.; Academic Press: Amsterdam, The Netherlands, 1998; 558p, ISBN 9780120932702.
38. Ryu, J.K.; Oh, J.H.; Kim, H.G.; Rhee, S.J.; Seo, M.; Jahng, G.H. Estimation of T2* Relaxation Times for the Glandular Tissue and Fat of Breast at 3T MRI System. *J. Korean Soc. Magn. Reson. Med.* **2014**, *18*, 1–6. [[CrossRef](#)]

39. Béalle, G.; Di Corato, R.; Kolosnjaj-Tabi, J.; Dupuis, V.; Clément, O.; Gazeau, F.; Wilhelm, C.; Ménager, C. Ultra magnetic liposomes for MR imaging, targeting, and hyperthermia. *Langmuir* **2012**, *28*, 11834–11842. [\[CrossRef\]](#)
40. Marie, H.; Lemaire, L.; Franconi, F.; Lajnef, S.; Frapart, Y.M.; Nicolas, V.; Frébourg, G.; Trichet, M.; Ménager, C.; Lesieur, S. Superparamagnetic Liposomes for MRI Monitoring and External Magnetic Field-Induced Selective Targeting of Malignant Brain Tumors. *Adv. Funct. Mater.* **2015**, *25*, 1258–1269. [\[CrossRef\]](#)
41. Garnier, B.; Tan, S.; Miraux, S.; Bled, E.; Brisson, A.R. Optimized synthesis of 100 nm diameter magnetoliposomes with high content of maghemite particles and high MRI effect. *Contrast Media Mol. Imaging* **2012**, *7*, 231–239. [\[CrossRef\]](#)
42. Carvalho, A.; Gonçalves, M.C.; Martins, M.B.F.; Meixedo, D.; Feio, G. Relaxivities of magnetoliposomes: The effect of cholesterol. *Magn. Reson. Imaging* **2013**, *31*, 610–612. [\[CrossRef\]](#)
43. Martínez-González, R.; Estelrich, J.; Busquets, M.A. Liposomes Loaded with Hydrophobic Iron Oxide Nanoparticles: Suitable T₂ Contrast Agents for MRI. *Int. J. Mol. Sci.* **2016**, *17*, 1209. [\[CrossRef\]](#) [\[PubMed\]](#)
44. Carvalho, A.; Gonçalves, M.C.; Corvo, M.L.; Martins, M.B.F. Development of New Contrast Agents for Imaging Function and Metabolism by Magnetic Resonance Imaging. *Magn. Reson. Insights* **2017**, *10*, 1178623X17722134. [\[CrossRef\]](#) [\[PubMed\]](#)
45. Mohamed, M.; Abu Lila, A.S.; Shimizu, T.; Alaaeldin, E.; Hussein, A.; Sarhan, H.A.; Szebeni, J.; Ishida, T. PEGylated liposomes: Immunological responses. *Sci. Technol. Adv. Mater.* **2019**, *20*, 710–724. [\[CrossRef\]](#) [\[PubMed\]](#)
46. Ren, X.; Zheng, R.; Fang, X.; Wang, X.; Zhang, X.; Yang, W.; Sha, X. Red blood cell membrane camouflaged magnetic nanoclusters for imaging-guided photothermal therapy. *Biomaterials* **2016**, *92*, 13–24. [\[CrossRef\]](#) [\[PubMed\]](#)
47. Philip, R.; Penzkofer, A.; Bäuml, W.; Szeimies, R.M.; Abels, C. Absorption and fluorescence spectroscopic investigation of indocyanine green. *J. Photochem. Photobiol. A* **1996**, *96*, 137–148. [\[CrossRef\]](#)
48. Beziere, N.; Lozano, N.; Nunes, A.; Salichs, J.; Queiros, D.; Kostarellos, K.; Ntziachristos, V. Dynamic imaging of PEGylated indocyanine green (ICG) liposomes within the tumor microenvironment using multi-spectral optoacoustic tomography (MSOT). *Biomaterials* **2015**, *37*, 415–424. [\[CrossRef\]](#)
49. Mérian, J.; Boisgard, R.; Bayle, P.A.; Bardet, M.; Tavitian, B.; Texier, I. Comparative biodistribution in mice of cyanine dyes loaded in lipid nanoparticles. *Eur. J. Pharm. Biopharm.* **2015**, *93*, 1–10. [\[CrossRef\]](#)
50. Sadauskas, E.; Wallin, H.; Stoltenberg, M.; Vogel, U.; Doering, P.; Larsen, A.; Danscher, G. Kupffer cells are central in the removal of nanoparticles from the organism. *Part. Fibre Toxicol.* **2007**, *4*, 10. [\[CrossRef\]](#)
51. Suganami, A.; Iwade, Y.; Shibata, S.; Yamashita, M.; Tanaka, T.; Shinozaki, N.; Aoki, I.; Saeki, N.; Shirasawa, H.; Okamoto, Y.; et al. Liposomally formulated phospholipid-conjugated indocyanine green for intra-operative brain tumor detection and resection. *Int. J. Pharm.* **2015**, *496*, 401–406. [\[CrossRef\]](#)
52. Zhao, P.; Zheng, M.; Yue, C.; Luo, Z.; Gong, P.; Gao, G.; Sheng, Z.; Zheng, C.; Cai, L. Improving drug accumulation and photothermal efficacy in tumor depending on size of ICG loaded lipid-polymer nanoparticles. *Biomaterials* **2014**, *35*, 6037–6046. [\[CrossRef\]](#)
53. Lee, C.H.; Cheng, S.H.; Wang, Y.J.; Chen, Y.C.; Chen, N.T.; Souris, J.; Chen, C.T.; Mou, C.Y.; Yang, C.S.; Lo, L.W. Near-Infrared Mesoporous Silica Nanoparticles for Optical Imaging: Characterization and In Vivo Biodistribution. *Adv. Funct. Mater.* **2009**, *19*, 215–222. [\[CrossRef\]](#)
54. Huang, J.; Shu, Q.; Wang, L.; Wu, H.; Wang, A.Y.; Mao, H. Layer-by-layer assembled milk protein coated magnetic nanoparticle enabled oral drug delivery with high stability in stomach and enzyme-responsive release in small intestine. *Biomaterials* **2015**, *39*, 105–113. [\[CrossRef\]](#) [\[PubMed\]](#)
55. Ashokan, A.; Gowd, G.S.; Somasundaram, V.H.; Bhupathi, A.; Peethambaran, R.; Unni, A.K.K.; Palaniswamy, S.; Nair, S.V.; Koyakutty, M. Multifunctional calcium phosphate nano-contrast agent for combined nuclear, magnetic and near-infrared in vivo imaging. *Biomaterials* **2013**, *34*, 7143–7157. [\[CrossRef\]](#) [\[PubMed\]](#)
56. Saxena, V.; Sadoqi, M.; Shao, J. Degradation kinetics of indocyanine green in aqueous solution. *J. Pharm. Sci.* **2003**, *92*, 2090–2097. [\[CrossRef\]](#) [\[PubMed\]](#)
57. Wang, H.; Li, X.; Tse, B.W.C.; Yang, H.; Thorling, C.A.; Liu, Y.; Touraud, M.; Chouane, J.B.; Liu, X.; Roberts, M.S.; et al. Indocyanine green-incorporating nanoparticles for cancer theranostics. *Theranostics* **2018**, *8*, 1227–1242. [\[CrossRef\]](#)
58. Sheng, Z.; Hu, D.; Zheng, M.; Zhao, P.; Liu, H.; Gao, D.; Gong, P.; Gao, G.; Zhang, P.; Ma, Y.; et al. Smart human serum albumin-indocyanine green nanoparticles generated by programmed assembly for dual-modal imaging-guided cancer synergistic phototherapy. *ACS Nano* **2014**, *8*, 12310–12322. [\[CrossRef\]](#)
59. Zheng, M.; Zhao, P.; Luo, Z.; Gong, P.; Zheng, C.; Zhang, P.; Yue, C.; Gao, D.; Ma, Y.; Cai, L. Robust ICG theranostic nanoparticles for folate targeted cancer imaging and highly effective photothermal therapy. *ACS Appl. Mater. Interfaces* **2014**, *6*, 6709–6716. [\[CrossRef\]](#)
60. Yan, F.; Wu, H.; Liu, H.; Deng, Z.; Liu, H.; Duan, W.; Liu, X.; Zheng, H. Molecular imaging-guided photothermal/photodynamic therapy against tumor by iRGD-modified indocyanine green nanoparticles. *J. Control. Release* **2016**, *224*, 217–228. [\[CrossRef\]](#)
61. Zhao, P.; Zheng, M.; Luo, Z.; Gong, P.; Gao, G.; Sheng, Z.; Zheng, C.; Ma, Y.; Cai, L. NIR-driven Smart Theranostic Nanomedicine for On-demand Drug Release and Synergistic Antitumour Therapy. *Sci. Rep.* **2015**, *5*, 14258. [\[CrossRef\]](#)
62. Galagudza, M.M.; Korolev, D.V.; Sonin, D.L.; Alexandrov, I.V.; Minasian, S.M.; Postnov, V.N.; Kirpicheva, E.B.; Papayan, G.V.; Uskov, I.S. Passive and active target delivery of drugs to ischemic myocardium. *Bull. Exp. Biol. Med.* **2011**, *152*, 105–107. [\[CrossRef\]](#)

-
63. Lipinski, M.J.; Albelda, M.T.; Frias, J.C.; Anderson, S.A.; Luger, D.; Westman, P.C.; Escarcega, R.O.; Hellinga, D.G.; Waksman, R.; Arai, A.E.; et al. Multimodality imaging demonstrates trafficking of liposomes preferentially to ischemic myocardium. *Cardiovasc. Resusc. Med.* **2016**, *17*, 106–112. [[CrossRef](#)]
 64. Paulis, L.E.; Geelen, T.; Kuhlmann, M.T.; Coolen, B.F.; Schäfers, M.; Nicolay, K.; Strijkers, G.J. Distribution of lipid-based nanoparticles to infarcted myocardium with potential application for MRI-monitored drug delivery. *J. Control. Release* **2012**, *162*, 276–285. [[CrossRef](#)] [[PubMed](#)]
 65. Yu, L.; Scherlag, B.S.; Dormer, K.; Rutel, I.; Huang, B.; Zhou, X.; Kuriakose, A.E.; Nguyen, K.K.; Po, S. Targeted Ganglionated Plexi Denervation Using Magnetic Nanoparticles Carrying Calcium Chloride Payload. *JACC Clin. Electrophysiol.* **2018**, *4*, 1347–1358. [[CrossRef](#)] [[PubMed](#)]